MATERIALS CHEMISTRY FRONTIERS

RESEARCH ARTICLE

View Article Online
View Journal | View Issue

Cite this: *Mater. Chem. Front.*, 2023, **7**, 1599

$[C_5H_{12}N]_2SnBr_6$: a lead-free phase transition compound with switchable quadratic nonlinear optical properties†

Xinxin Hu,[ab] Haojie Xu,[ab] Wuqian Guo,[ab] Shiguo Han,[a] Yi Liu,[a] Yu Ma,[ab] Qingshun Fan,[ab] Junhua Luo [a] and Zhihua Sun *[ac]

Solid-state phase transition materials with tunable quadratic nonlinear optical (NLO) properties under different states hold great potential applications in a wide range of fields. Despite great efforts, lead-free organic–inorganic hybrid NLO switchable materials are still scarce. Here, we report a new lead-free organic–inorganic hybrid compound $(NMP)_2SnBr_6$ (**1**, where NMP is *N*-methylpyrrolidinium) which adopts the zero-dimensional perovskite-like motif. It demonstrates a structural phase transition at T_c = 352 K, as confirmed by differential scanning calorimetry and specific heat measurements. Single-crystal structure analyses at different temperatures indicate the occurrence of symmetry breaking from *Pbam* (at 360 K, > T_c) to *Pba*2 (at 300 K, < T_c), which can be attributed to the configuration changes of organic *N*-methylpyrrolidinium cations. In particular, **1** shows remarkable NLO signal contrast up to ~25 and excellent switching stability after multiple heating–cooling cycles, suggesting its potential application as a switchable NLO material. This work paves the way for exploring new organic–inorganic hybrid functional materials.

Received 22nd December 2022,
Accepted 7th February 2023

DOI: 10.1039/d2qm01340a

rsc.li/frontiers-materials

Introduction

Stimuli-responsive materials are those substances which can respond to external stimuli, such as temperature, light, and external magnetic and electric fields.[1–7] The physical properties of these materials can be changed significantly between different states. These switching properties have been applied in a wide range of applications such as lasers, memorizers and switches, thereby attracting great interest.[8–11] Among them, switchable NLO properties have become an important research topic in condensed matter science.[12] Previous studies revealed that the switchable NLO properties can be realized by various strategies, in which one of the efficient ways is to introduce flexible organic cations into inorganic frameworks.[13] The flexible organic counterparts in the organic–inorganic hybrid system are favorable to molecular motions, including order–disorder transformation, reorientational and rotational motion, which are tightly associated with the switchable NLO properties of phase transition materials.[14–18] For example, in (*N*-methylpyrrolidinium)$PbBr_3$,[19] phase transition can be mainly attributed to the order–disorder transformation of flexible *N*-methylpyrrolidinium cations. Other reported studies on bis(cyclohexylaminium)-tetrabromo lead and [*N*-methylpiperidinium]PbI_3 also show order–disorder phase transition and corresponding excellent tunable NLO properties, which benefit from the reorientation of organic moieties and inorganic parts.[20,21] These findings disclose that phase transition compounds with tunable NLO properties could be feasibly tailored through incorporation of flexible organic molecules into the framework of hybrid compounds.[22,23]

Organic–inorganic hybrid compounds combine advantages of both organic and inorganic components at the molecular level.[24–26] Within this system, organic moieties endow structural diversity and dynamic characteristics, which are favorable to the design of phase transition materials with tunable NLO properties.[22,27] As an important family of organic components, annular organic cations play a key role in the design of phase transition materials with tunable NLO properties.[28,29] For example, organic–inorganic hybrids of $(CHA)_2PbBr_{4-4x}I_{4x}$, (benzylammonium)$_2PbCl_4$ and (pyrrolidinium)$CdCl_3$ show excellent switchable NLO properties.[30–32] Despite great efforts, reports on phase transition materials with tunable NLO properties in the family of organic–inorganic hybrids are still scarce,

[a] *State Key Laboratory of Structural Chemistry, Fujian Institute of Research on the Structure of Matter, Chinese Academy of Sciences, Fuzhou, Fujian 350002, China. E-mail: sunzhihua@fjirsm.ac.cn*
[b] *University of Chinese Academy of Sciences, Beijing 100049, China*
[c] *Fujian Science & Technology Innovation Laboratory for Optoelectronic Information of China, Fuzhou, Fujian 350108, P. R. China*

† Electronic supplementary information (ESI) available. CCDC 2210039 and 2210040. For ESI and crystallographic data in CIF or other electronic format see DOI: https://doi.org/10.1039/d2qm01340a

and most of these organic–inorganic hybrid dielectric switchable compounds contain metal lead, which can cause damage to the environment and limit their commercial applications. Moreover, the majority of tunable NLO materials in the organic–inorganic hybrid system are formed by order–disorder type phase transformation. Therefore, it is highly desirable to explore new phase transition materials with tunable NLO properties by virtue of a complementary strategy.

Here, we report a new zero-dimensional lead-free hybrid compound by incorporating organic *N*-methylpyrrolidinium (NMP) with the Sn–Br inorganic framework, ($[NMP]_2SnBr_6$, **1**), showing a reversible structural phase transition at T_1 = 352 K upon heating as confirmed by differential scanning calorimetry. Emphatically, it shows a remarkable NLO signal contrast up to ~25, suggesting its potential application as a switchable NLO material. After multiple heating–cooling cycles, **1** still shows great switchable NLO and dielectric stability. Such switchable responses of **1** can be mainly attributed to the configuration changes of organic cations. This work paves the way for exploring new functional materials with NLO switching properties.

Experimental section

Synthesis

All chemical ingredients are commercially purchased without any purification. 10 mL HBr solution and 0.5 g SnO were put in a 50 mL round-bottom beaker. After that, the mixture was stirred for 1 hour to form a transparent solution. 0.5 mL *N*-methylpyrrodine was then added into the beaker. Next, the mixture was heated and stirred for 30 minutes to form a clear solution. Crystals of **1** were obtained after two weeks by slowly evaporating the solution at ambient temperature. The purity of crystals was confirmed through powder X-ray diffraction analyses, and the measured data were in accordance with the simulated patterns obtained from its single-crystal structure.

Thermal measurements

Pure crystals of **1** were chosen to carry out thermal measurements using differential scanning calorimetry (DSC) (NETZCHSCH DSC 3500). Both the heating and cooling rates were fixed at 5 K per minute in the temperature range between 315 K and 360 K. The measurement was performed under atmospheric pressure with nitrogen gas. Specific heat (C_p) was measured upon a heating mode based on the sapphire standard.

Single-crystal structure analyses

Single-crystal X-ray diffraction data of **1** at 300 K was obtained using a Rigaku CCD diffractometer with Ga-Kα radiation of wavelength 1.3405 Å. A Bruker D8 diffractometer with Mo-Kα of wavelength 0.71073 Å was used to obtain the structural data of **1** at 360 K. All the crystal structures were solved using the Olex2 software package using the intrinsic phasing method of the ShelXT program. All atoms except H were refined using an anisotropic method. All hydrogen atoms in the structures were geometrically generated using the software of Olex2. A detailed description of crystal structures of **1** is presented in Table S1 (ESI†). And all crystallographic data were uploaded to The Cambridge Crystallographic Data Center (CCDC) with numbers 2210039 and 2210040,† respectively.

Dielectric measurements

Silver was covered on the surface of single crystals of **1** to fabricate electrodes. Dielectric experiments were then carried out to measure the complex dielectric permittivity in the temperature range of 330–370 K. The frequency was set at 1 MHz and the AC voltage was fixed at 1 V.

Second harmonic generation (SHG) signal measurements

Variable-temperature measurements of SHG signals were performed using an Nd:YAG laser with incident wavelength of 1064 nm. Standard KH_2PO_4 was used as a reference and treated using the same procedure. The ground powder of **1** was compressed to tablets for the SHG signal measurements.

Powder X-ray diffraction measurement (PXRD)

The powder X-ray diffraction pattern of **1** was recorded on a Powder X-Ray Diffractometer (MiniFlex 600). The measurement was performed in the 2-theta range between 5° to 40° at room temperature.

Theoretical calculation analyses

Theoretical calculation analyses of single-crystal structure of **1** were performed using Cambridge Sequential Total Energy Package (CASTEP) under the DFT method. The exchange-correlation potential was calculated using Perdew–Burke–Ernzerhof method for solid functions using the approximation method of GGA. The norm-conserving pseudopotential was used to characterize the interactions between ionic cores and electrons. The energy cutoff for the plane-wave basis was fixed at 500 eV.

Results and discussion

Phase transition properties

DSC and C_p measurements were effective ways used to investigate the thermal properties of phase transition materials. The structure phase transition of compounds was generally accompanied by thermal entropy changes, which can be confirmed in the heating and cooling process of DSC measurements. Here, the reversible endothermic and exothermic anomalies appeared at 352 K upon heating mode and 333 K upon cooling, which reveal the phase transition properties of **1** (Fig. 1a). In the DSC curves, the large thermal hysteresis (19 K) and sharp anomalies indicate its first order phase transition. The peak-like anomaly in C_p also corresponds well with the results of DSC (Fig. 1b). The enthalpy change (ΔH) and entropy change (ΔS) in the heating mode can be calculated from the C_p–T curve as 890.7 J mol^{-1} and 2.53 J mol^{-1} K^{-1}, respectively. According to the Boltzmann equation $\Delta S = R\ln N$, in which N is the ratio of

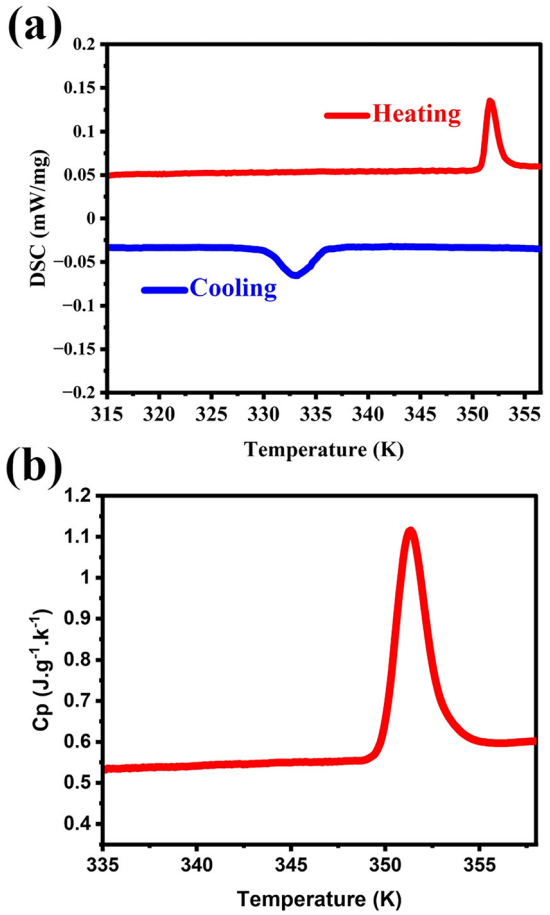

Fig. 1 (a) DSC curves under the heating and cooling modes and (b) c_p curve in the heating mode.

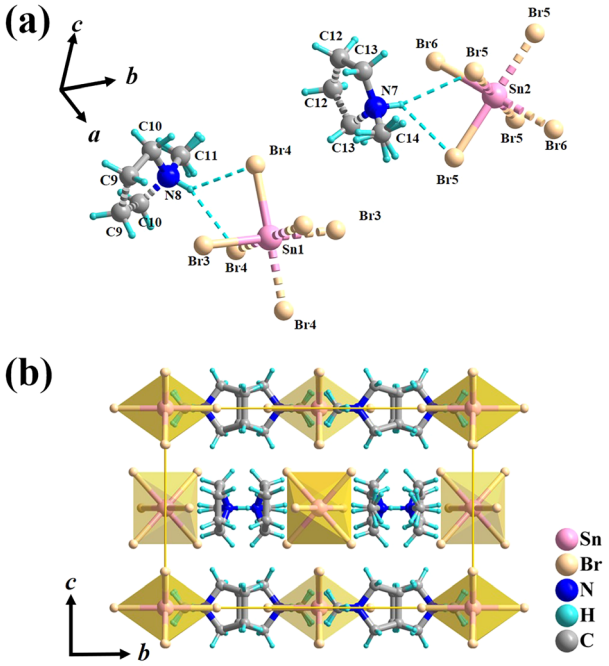

Fig. 2 (a) Asymmetric unit and (b) packing view of **1** along *a*-axis at 360 K. Dashed lines are used to link equivalent atoms generated by the symmetry operation except cyan dashed lines used to represent hydrogen bonds.

orientations between different phases and R is the molar gas constant, N is calculated as 1.36, revealing the complexity of the phase transition of **1**, instead of simple order–disorder transition (calculation is provided in the ESI†).

Crystal structure analyses

X-ray single-crystal diffraction analyses were performed to determine the microscopic mechanism of structural changes of **1** at two different temperatures, *i.e.*, low temperature phase (LTP) at 300 K (below T_c) and high temperature phase (HTP) at 360 K (above T_c). The results reveal that **1** crystallizes in the same orthorhombic system but different space groups in different phases. In HTP, **1** crystallizes in a centric space group of *Pbam*. The cell parameters at HTP are $\alpha = \gamma = \beta = 90^\circ$, a = 13.9302 (10), b = 15.5956 (9), c = 10.1118 (8), V = 2196.8 (3) and Z = 4, as given in Table S1 (ESI†). The asymmetric unit of **1** consists of protonated NMP cations and anionic $[SnBr_6]^{2-}$ octahedra in the HTP, as shown in Fig. 2a. Partial hydrogen atoms of NMP anions are disordered with atoms located at two possible equilibrium positions. The disorder characteristics can also be revealed by the thermal ellipsoids of atoms of NMP cation, in which the large thermal ellipsoids of C and N atoms indicate the average effect of the disordered atoms (Fig. S3, ESI†).[33] Intermolecular H-bonding distances between protonated N atoms of NMP cations and Br atoms of $[SnBr_6]^{2-}$ anions are measured as 2.736 Å and 2.900 Å (Fig. S4, ESI†). All components of **1** show symmetric configurations with respect to their mirror planes due to highly crystallographic symmetry (Fig. 2b). In both phases, no significant changes for $SnBr_6$ octahedrons are observed, whereas the distorted configuration of NMP cations can be observed in LTP. As the temperature decreased below T_c, crystal structure of **1** transforms into the non-centrosymmetric phase with the space group of *Pba*2 and point group of C_{2v}. The cell parameters for this acentric structure are $\alpha = \gamma = \beta = 90^\circ$, a = 15.5317 (4), b = 13.8674 (3), c = 10.0184, V = 2157.39 (10) and Z = 4 (Table S1, ESI†). The changes in the cell volume and axes lengths suggest the emergence of phase transition. Meanwhile, the distorted NMP cations with N atoms moving toward the same direction of the crystallographic *c*-axis results in the disappearance of *c*-mirror plane and symmetry breaking. This structural transition means that the number of symmetric elements of **1** is halved from eight in the HTP to four in the LTP, as illustrated in Fig. 3.[34] The asymmetric unit of **1** at LTP comprises two protonated NMP cations and two half-$[SnBr_6]^{2-}$ anions, as shown in Fig. 4a. Each Sn atom is coordinated with six Br atoms, forming an octahedral geometry. The organic cations are linked with the octahedral $[SnBr_6]^{2-}$ anions by N–H···Br hydrogen bonds (Fig. S4, ESI†). The bond lengths of Sn–Br are in the range of 2.593 to 2.607 Å, almost the same as those (2.5936 to 2.602 Å) in the HTP (Tables S2 and S3, ESI†). The angles of Br–*Sn*–Br are in the range of 88.05° to 91.4°, exhibiting slight deviation from the standard octahedral angle of 90°. In LTP, the hydrogen bond

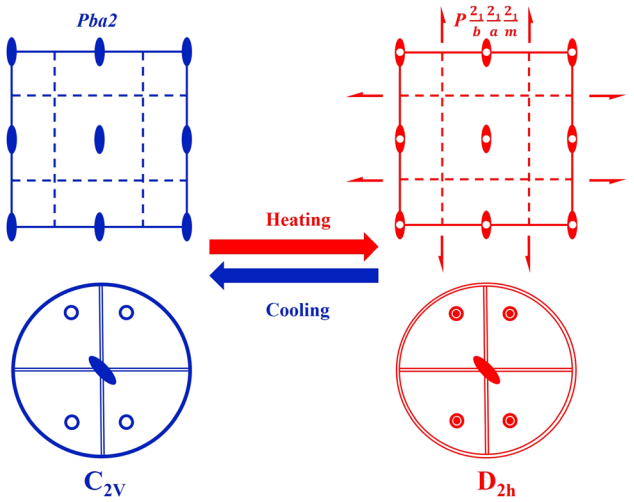

Fig. 3 Transformation of spatial symmetry operations of **1** during the phase transition.

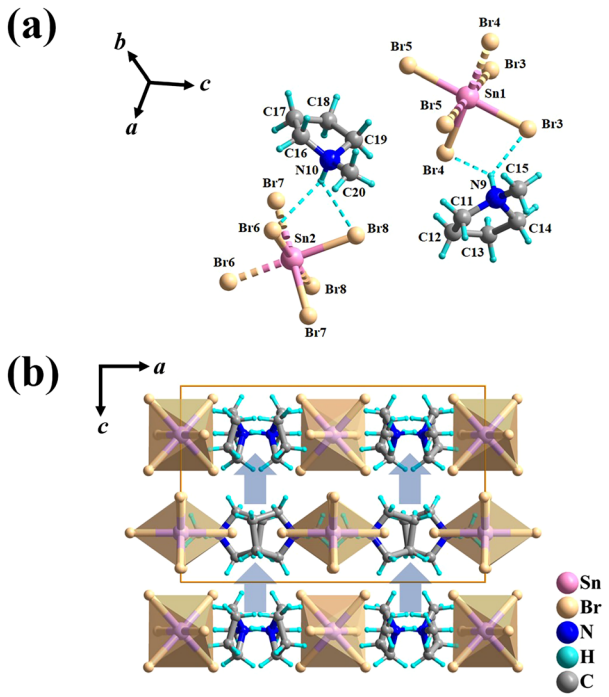

Fig. 4 (a) Asymmetric unit and (b) packing view of the unit cell along the *b*-axis at 300 K. Dashed lines were used to link equivalent atoms except cyan dashed lines used to represent hydrogen bonds.

lengths of N–H···Br are 2.642 Å to 2.930 Å. The difference between the structure at HTP and LTP is that organic NMP cations show distorted configurations and orient along the crystallographic *c*-axis, which contribute to the acentric structure, as shown in Fig. 4b.[35] The acentric structure was further confirmed by the measurement of SHG signals (Fig. 6b).

The above studies reveal that between the HTP and LTP, no significant change was discovered in the inorganic $SnBr_6$ octahedra, whereas the N atoms of NMP cations show obvious displacements. In detail, the N atoms of NMP cations deviate its *c*-mirror planes existing in HTP and reorientate toward the *c*-axis direction in LTP, leading to the structure phase transition.

Band structure analyses

First principles DFT calculation was performed to analyze the electronic properties of **1**. As shown in Fig. 5a, the lowest point of the conduction band and the highest point of the valence band are located at different points (G and Z, respectively), revealing the indirect bandgap characteristics of **1**. Its bandgap is calculated as 2.76 eV, corresponding well with the experimental value (2.68 eV) obtained from the UV-vis absorption spectrum as shown in Fig. S2 (ESI†). The calculated distribution of partial density of states (PDOS) indicates the overlapped energy regions of $C_{2s/p}$, $N_{2s/p}$ and H_{1s} states are far away from the Fermi level due to strong covalent interactions of C–H and N–H bonds (Fig. 5b). However, the density states of $Br_{4s/p}$ and $Sn_{5s/p}$ are distributed near the Fermi level, determining the minimum of the conduction band and the maximum of the valence band. Those results denote that its band gap mainly stems from the electron distribution of inorganic components, resembling some previously reported materials such as $(PEA)_2PbI_4$.[36] This is also revealed by the calculated charge-density distribution of **1** as shown in Fig. S5 (ESI†).

Switchable dielectric and NLO properties

Generally, abrupt changes of physical properties of phase transition materials can be observed in the vicinity of T_c due

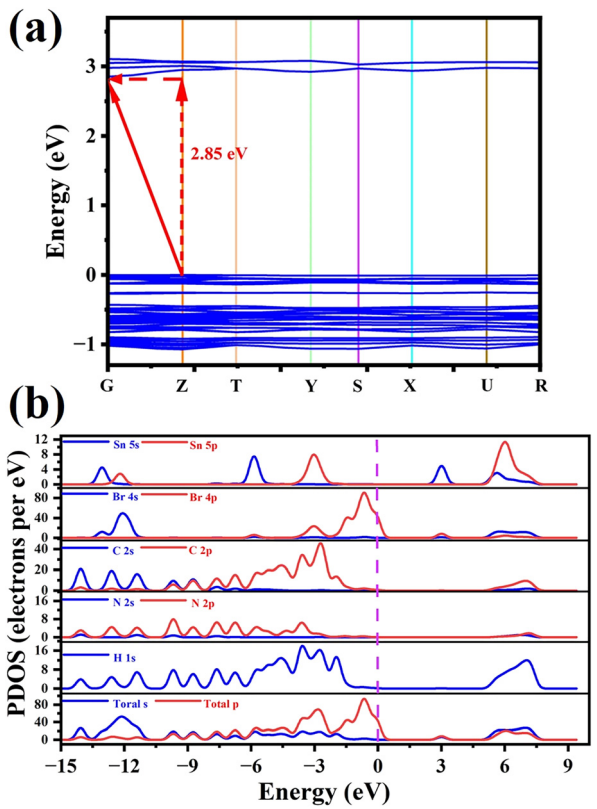

Fig. 5 (a) Calculated bandgap and (b) PDOS spectra of **1**.

to the structural changes. Here, variable-temperature dielectric properties of **1** were measured along different axes using single crystals. As shown in Fig. 6a, the real parts (ε') of dielectric constants along three crystallographic axes keep virtually stable below T_c, matching with the low-dielectric state of **1**. With temperature increasing to its T_c, obvious step-like changes in dielectric constant emerge along different crystallographic axes. Interesting, the ε' value measured along *c*-axis is the highest in the high-dielectric state, in contrast with the lowest ε' value along its *a*-axis. The difference in dielectric changes probably ascribes to the configuration changes of NMP cations, that is, the disappearance of the *c*-mirror and related symmetry breaking along the crystallographic *c*-direction (Fig. 6c). This dielectric transformation between different states resembles that of some switchable NLO materials, such as (hexamethyleneimine)$_2$BiBr$_5$ and $(C_3H_8N_2)_2SbBr_5$.[37,38] With the increasing temperature, **1** shows a dramatic variation of quadratic SHG signals, indicating the structural change of **1** from a non-centrosymmetric state (SHG-on) to a centrosymmetric one (SHG-off), as shown in Fig. 6b. The remarkable NLO signal

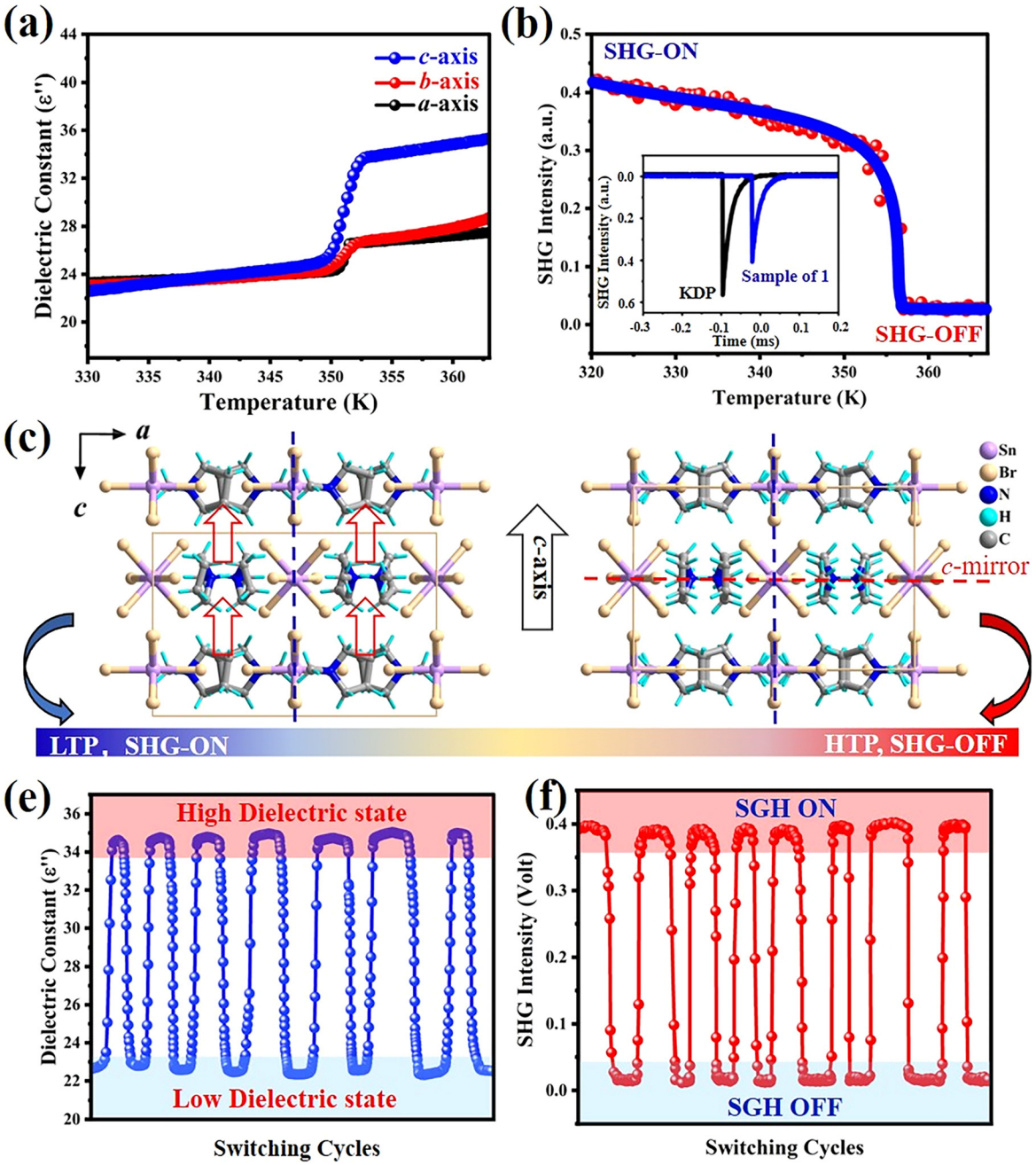

Fig. 6 (a) Variable-temperature dielectric constants of three crystallographic axes and (b) SHG signals. Inset: Oscilloscope traces of SHG signals of **1** compared with the reference KDP. (c) Schematic diagram of the appearance of symmetry breaking (e) switchable dielectric and (f) SHG properties after multiple heating–cooling cycles.

contrast of ~25 can be calculated between its SHG-on and SHG-off states, suggesting its potential applications in a switchable NLO field.[39] The contrast figure of ~25 is much higher than that of most NLO switching materials (liquids and solids), and is comparable with $(Hdabco^{+})(CF_3COO^{-})$ and $NH_4[(CH_3)_4N]SO_4{\cdot}H_2O$.[40,41] Stability is an important factor for evaluating the potentials of functional materials. Therefore, the reversible properties of **1** were measured using crystal samples of **1**. As shown in Fig. 6e, the dielectric responses can recover after at least 7 heating–cooling cycles without any attenuation. This reveals its great stability after repeating structure transformation. Furthermore, variable-temperature SHG measurements were carried out to confirm the switchable SHG responses. Similarly, the SHG signal responses show great anti-fatigue merit between its SHG-on and SHG-off states after multiple heating–cooling runs (Fig. 6f). Our further measurements reveal its SHG signals still retain rapid responses without any obvious suppression, even under long-time irradiation. These results suggest the great stability of **1**, which affords its great potential applications as a NLO switching material.

Conclusions

In summary, we have successfully explored a new lead-free organic–inorganic hybrid compound $[NMP]_2SnBr_6$. It demonstrates a structural phase transition along with the occurrence of symmetry breaking from *Pbam* to *Pba*2. The mechanism is ascribed to the symmetry configuration changes of organic cations, which differs from the majority of known NLO-switching systems. In particular, it shows distinct switchable NLO properties with a remarkable NLO signal contrast of up to ~25. The contrast is larger than those of many other NLO switching materials. It also exhibits great dielectric and NLO stability after multiple cycles. These properties suggest its great potential application as a switchable NLO material. This work paves the way for exploring new organic–inorganic hybrid functional materials.

Author contributions

Xinxin Hu carried out the experiments and wrote the manuscript. Haojie Xu and Wuqian Guo performed the characterization of compounds. Yi Liu performed theoretical calculations, and Shiguo Han analyzed the result of theoretical calculations. Yu Ma and Qingshun Fan measured the SHG signals. Junhua Luo provided suggestions on the manuscript writing. Zhuhua Sun conceived the idea and supervised the project.

Conflicts of interest

There are no conflicts to declare.

Acknowledgements

The authors thank Aurang Zeb for help with experiments. This work was financially supported by the National Natural Science Foundation of China (22125110, 21875251, 21833010, and U21A2069), the Fujian Science & Technology Innovation Laboratory for Optoelectronic Information of China (2021ZR126), the Key Research Program of Frontier Sciences of the Chinese Academy of Sciences (ZDBS-LY-SLH024), the National Postdoctoral Program for Innovative Talents (BX2021315), and the National Key Research and Development Program of China (2019YFA0210402).

References

1 Y. Q. Shi, C. Zhang, H. Zhang, J. H. Bechtel, L. R. Dalton, B. H. Robinson and W. H. Steier, Low (Sub-1-Volt) Halfwave Voltage Polymeric Electro-Optic Modulators Achieved by Controlling Chromophore Shape, *Science*, 2000, **288**, 119–122.
2 M. Lee, H. E. Katz, C. Erben, D. M. Gill, P. Gopalan, J. D. Heber and D. J. McGee, Broadband Modulation of Light by Using An Electro-Optic Polymer, *Science*, 2002, **298**, 1401–1403.
3 F. Castet, V. Rodriguez, J. L. Pozzo, L. Ducasse, A. Plaquet and B. Champagne, Design and Characterization of Molecular Nonlinear Optical Switches, *Acc. Chem. Res.*, 2013, **46**, 2656–2665.
4 M. A. C. Stuart, W. T. S. Huck, J. Genzer, M. Muller, C. Ober, M. Stamm, G. B. Sukhorukov, I. Szleifer, V. V. Tsukruk, M. Urban, F. Winnik, S. Zauscher, I. Luzinov and S. Minko, Emerging Applications of Stimuli-Responsive Polymer Materials, *Nat. Mater.*, 2010, **9**, 101–113.
5 S. Horike, S. Shimomura and S. Kitagawa, Soft Porous Crystals, *Nat. Chem.*, 2009, **1**, 695–704.
6 H. J. Xu, W. Q. Guo, J. Q. Wang, Y. Ma, S. G. Han, Y. Liu, L. Lu, X. Pan, J. H. Luo and Z. H. Sun, A Metal-Free Molecular Antiferroelectric Material Showing High Phase Transition Temperatures and Large Electrocaloric Effects, *J. Am. Chem. Soc.*, 2021, **143**, 14379–14385.
7 Y. Y. Tang, J. C. Liu, Y. L. Zeng, H. Peng, X. Q. Huang, M. J. Yang and R. G. Xiong, Optical Control of Polarization Switching in a Single-Component Organic Ferroelectric Crystal, *J. Am. Chem. Soc.*, 2021, **143**, 13816–13823.
8 Y. L. Yu, M. Nakano and T. Ikeda, Directed Bending of a Polymer Film by Light - Miniaturizing A Simple Photomechanical System Could Expand Its Range of Applications, *Nature*, 2003, **425**, 145.
9 J. A. Delaire and K. Nakatani, Linear and Nonlinear Optical Properties of Photochromic Molecules and Materials, *Chem. Rev.*, 2000, **100**, 1817–1845.
10 M. Samoc, N. Gauthier, M. P. Cifuentes, F. Paul, C. Lapinte and M. G. Humphrey, Electrochemical Switching of the Cubic Nonlinear Optical Properties of an Aryldiethynyl-Linked Heterobimetallic Complex Between Three Distinct States, *Angew. Chem., Int. Ed.*, 2006, **45**, 7376–7379.
11 M. Wuttig and N. Yamada, Phase-Change Materials for Rewriteable Data Storage, *Nat. Mater.*, 2007, **6**, 824–832.
12 W. Zhang, Y. Cai, R. G. Xiong, H. Yoshikawa and K. Awaga, Exceptional Dielectric Phase Transitions in a Perovskite-Type Cage Compound, *Angew. Chem., Int. Ed.*, 2010, **49**, 6608–6610.

13 L. Li, Z. Sun, P. Wang, W. Hu, S. Wang, C. Ji, M. Hong and J. Luo, Tailored Engineering of An Unusual $(C_4H_9NH_3)_2$-$(CH_3NH_3)_2Pb_3Br_{10}$ Two-Dimensional Multilayered Perovskite Ferroelectric for A High-Performance Photodetector, *Angew. Chem., Int. Ed.*, 2017, **56**, 12150–12154.
14 M. Ptak, M. Maczka, A. Gagor, A. Sieradzki, A. Stroppa, D. Di Sante, J. M. Perez-Mato and L. Macalik, Experimental and Theoretical Studies of Structural Phase Transition in A Novel Polar Perovskite-Like C2H5NH3 Na0.5Fe0.5(HCOO)(3) Formate, *Dalton Trans.*, 2016, **45**, 2574–2583.
15 P. Zhou, Z. H. Sun, S. Q. Zhang, C. M. Ji, S. G. Zhao, R. G. Xiong and J. H. Luo, A Sequentially Switchable Molecular Dielectric Material Tuned by the Stepwise Ordering in Diisopropylammonium Trifluoromethanesulfonate, *J. Mater. Chem. C*, 2014, **2**, 2341–2345.
16 S. Y. Zeng, Z. H. Sun, C. M. Ji, S. Q. Zhang, C. Song and J. H. Luo, Dibenzylammonium trichloroacetate: an above-room-temperature order-disorder switchable dielectric material, *CrystEngComm*, 2016, **18**, 3606–3611.
17 Z. X. Wang, W. Q. Liao, H. Y. Ye and Y. Zhang, Sequential Structural Transitions with Distinct Dielectric Responses in A Layered Perovskite Organic-Inorganic Hybrid Material: $(C_4H_9N)_2$ $PbBr_4$, *Dalton Trans.*, 2015, **44**, 20406–20412.
18 W. Zhang, H. Y. Ye, R. Graf, H. W. Spiess, Y. F. Yao, R. Q. Zhu and R. G. Xiong, Tunable and Switchable Dielectric Constant in an Amphidynamic Crystal, *J. Am. Chem. Soc.*, 2013, **135**, 5230–5233.
19 Q. Fan, Y. Ma, H. Xu, Y. Song, Y. Liu, J. Luo and Z. Sun, Near-Room-Temperature Reversible Switching of Quadratic Optical Nonlinearities in A One-Dimensional Perovskite-Like Hybrid, *Microstructures*, 2022, **2**, 2022013.
20 Z. H. Sun, X. T. Liu, T. Khan, C. M. Ji, M. A. Asghar, S. E. Zhao, L. N. Li, M. C. Hong and J. H. Luo, A Photoferroelectric Perovskite-Type Organometallic Halide with Exceptional Anisotropy of Bulk Photovoltaic Effects, *Angew. Chem., Int. Ed.*, 2016, **55**, 6545–6550.
21 H. Y. Zhang, X. G. Chen, Z. X. Zhang, X. J. Song, T. Zhang, Q. Pan, Y. Zhang and R. G. Xiong, Methylphosphonium Tin Bromide: A 3D Perovskite Molecular Ferroelectric Semiconductor, *Adv. Mater.*, 2020, **32**, e2005213.
22 W. Q. Guo, X. T. Liu, S. G. Han, Y. Liu, Z. Y. Xu, M. C. Hong, J. H. Luo and Z. H. Sun, Room-Temperature Ferroelectric Material Composed of A Two-Dimensional Metal Halide Double Perovskite for X-ray Detection, *Angew. Chem., Int. Ed.*, 2020, **59**, 13879–13884.
23 W. Zhang and R. G. Xiong, Ferroelectric Metal-Organic Frameworks, *Chem. Rev.*, 2012, **112**, 1163–1195.
24 B. Saparov and D. B. Mitzi, Organic-Inorganic Perovskites: Structural Versatility for Functional Materials Design, *Chem. Rev.*, 2016, **116**, 4558–4596.
25 Z. Y. Du, T. T. Xu, B. Huang, Y. J. Su, W. Xue, C. T. He, W. X. Zhang and X. M. Chen, Switchable Guest Molecular Dynamics in A Perovskite-Like Coordination Polymer Toward Sensitive Thermoresponsive Dielectric Materials, *Angew. Chem., Int. Ed.*, 2015, **54**, 914–918.
26 W. Q. Liao, Y. Y. Tang, P. F. Li, Y. M. You and R. G. Xiong, Large Piezoelectric Effect in A Lead-Free Molecular Ferroelectric Thin Film, *J. Am. Chem. Soc.*, 2017, **139**, 18071–18077.
27 S. Han, G.-E. Wang, G. Xu, J. Luo and Z. Sun, Ferroelectric Perovskite-Type Films with Robust in-Plane Polarization Toward Efficient Room-Temperature Chemiresistive Sensing, *Fundam. Res.*, 2022, DOI: **10.1016/j.fmre.2022.01.015**.
28 L. Mao, C. C. Stoumpos and M. G. Kanatzidis, Two-Dimensional Hybrid Halide Perovskites: Principles and Promises, *J. Am. Chem. Soc.*, 2019, **141**, 1171–1190.
29 C. R. Huang, X. Z. Luo, X. G. Chen, X. J. Song, Z. X. Zhang and R. G. Xiong, A Multiaxial Lead-Free Two-Dimensional Organic-Inorganic Perovskite Ferroelectric, *Natl. Sci. Rev.*, 2021, **8**, nwaa232.
30 H. Y. Ye, W. Q. Liao, C. L. Hu, Y. Zhang, Y. M. You, J. G. Mao, P. F. Li and R. G. Xiong, Bandgap Engineering of Lead-Halide Perovskite-Type Ferroelectrics, *Adv. Mater.*, 2016, **28**, 2579.
31 W. Q. Liao, Y. Zhang, C. L. Hu, J. G. Mao, H. Y. Ye, P. F. Li, S. D. Huang and R. G. Xiong, A Lead-Halide Perovskite Molecular Ferroelectric Semiconductor, *Nat. Commun.*, 2015, **6**, 7338.
32 Y. Y. Tang, Y. Ai, W. Q. Liao, P. F. Li, Z. X. Wang and R. G. Xiong, H/F-Substitution-Induced Homochirality for Designing High-T_c Molecular Perovskite Ferroelectrics, *Adv. Mater.*, 2019, **31**, e1902163.
33 Y. Zhang, W. Zhang, S. H. Li, Q. Ye, H. L. Cai, F. Deng, R. G. Xiong and S. D. Huang, Ferroelectricity Induced by Ordering of Twisting Motion in A Molecular Rotor, *J. Am. Chem. Soc.*, 2012, **134**, 11044–11049.
34 H. Fuess, T. Hahn, H. Wondratschek, U. Müller, U. Shmueli, E. Prince, A. Authier, V. Kopský, D. B. Litvin, M. G. Rossmann, E. Arnold, S. R. Hall, B. McMahon and T. Hahn, *The International Tables for Crystallography*, Springer, Dordrecht, 2006.
35 X. Hu, H. Xu, Y. Liu, L. Lu, W. Guo, S. Han, J. Luo and Z. Sun, Incorporating an Aromatic Cationic Spacer to Assemble 2D Polar Perovskite Crystals Toward Self-Powered Detection of Quite Weak Polarized Light, *J. Phys. Chem. Lett.*, 2022, **13**, 6017–6023.
36 Y. Liu, H. Ye, Y. Zhang, K. Zhao, Z. Yang, Y. Yuan, H. Wu, G. Zhao, Z. Yang, J. Tang, Z. Xu and S. Liu, Surface-Tension-Controlled Crystallization for High-Quality 2D Perovskite Single Crystals for Ultrahigh Photodetection, *Matter*, 2019, **1**, 465–480.
37 J. Zhang, S. G. Han, X. T. Liu, C. M. Ji, K. W. Tao, M. A. Asghar, J. H. Luo and Z. H. Sun, Successive Near-Room-Temperature Dielectric Phase Transitions in a Lead-Free Hybrid Perovskite-Like Compound, *Inorg. Chem. Front.*, 2019, **6**, 233–237.
38 M. Li, B. Teng, S. Han, T. Yang, Y. Li, Y. Liu, X. Zhang, X. Liu, J. Luo and Z. Sun, Near-Room-Temperature Tunable Dielectric Response Induced by Dual Phase Transitions in a Lead-Free Hybrid: (C3H8N)2SbBr5, *CrystEngComm*, 2019, **21**, 3740–3744.
39 P. Serra-Crespo, M. A. van der Veen, E. Gobechiya, K. Houthoofd, Y. Filinchuk, C. E. Kirschhock, J. A. Martens,

B. F. Sels, D. E. De Vos, F. Kapteijn and J. Gascon, NH_2-MIL-53(Al): A High-Contrast Reversible Solid-State Nonlinear Optical Switch, *J. Am. Chem. Soc.*, 2012, **134**, 8314–8317.

40 Z. Sun, J. Luo, S. Zhang, C. Ji, L. Zhou, S. Li, F. Deng and M. Hong, Solid-State Reversible Quadratic Nonlinear Optical Molecular Switch with an Exceptionally Large Contrast, *Adv. Mater.*, 2013, **25**, 4159–4163.

41 S. Liu, Z. Sun, C. Ji, L. Li, S. Zhao and J. Luo, Exceptional Bi-Step Switching of Quadratic Nonlinear Optical Properties in a One-Dimensional Channel Compound, *Chem. Commun.*, 2017, **53**, 7669–7672.

